Correspondence to:

A. Samin,
apolline.samin@uib.no

Author Contributions:

Conceptualization: Apolline Samin, Desiree L. Roerdink, Eoghan P. Reeves, Olivier Rouxel
Formal analysis: Apolline Samin, Eoghan P. Reeves, Johannes Scheffler, Wolfgang Bach, Andreas Beinlich
Investigation: Apolline Samin, Eoghan P. Reeves, Johannes Scheffler, Andreas Beinlich, John W. Jamieson
Methodology: Olivier Rouxel
Resources: Eoghan P. Reeves, Wolfgang Bach, Olivier Rouxel

Preservation of Hydrothermal Fluid Copper Isotope Signatures in Chalcopyrite-Rich Chimneys: A Case Study From the PACMANUS Vent Field, Manus Basin

Apolline Samin[1], Desiree L. Roerdink[1], Eoghan P. Reeves[1,2], Johannes Scheffler[1], Wolfgang Bach[2], Andreas Beinlich[1,3], John W. Jamieson[4], and Olivier Rouxel[5]

[1]Department of Earth Science and Centre for Deep Sea Research, University of Bergen, Bergen, Norway, [2]MARUM-Center for Marine Environmental Sciences & Department of Geosciences, University of Bremen, Bremen, Germany, [3]Institute of Geological Sciences, Freie Universität Berlin, Berlin, Germany, [4]Department of Earth Science, Memorial University of Newfoundland, St. John's, NL, Canada, [5]Department of Marine Geosciences, IFREMER, Plouzané, France

Abstract Copper isotopes ($\delta^{65}Cu$) in hydrothermal fluids have the potential to provide information on ore-forming processes occurring below the seafloor, but Cu isotope data from high-temperature fluids are scarce. Here, we examine the extent to which coexisting sulfide minerals in a hydrothermal chimney can preserve fluid Cu isotope ratios using a fluid-solid pair of a black smoker (333°C) from the Roman Ruins vent area (PACMANUS) in the Manus Basin. Two ca. 3 cm long transects through the chalcopyrite-rich chimney wall show an increase in $\delta^{65}Cu$ from 0.48 to 2.28‰ from the interior to the exterior, coupled with limited variation in sulfide $\delta^{34}S$ (1.52–4.72‰). The Cu isotopic composition of chalcopyrite from the innermost wall closely resembles the $\delta^{65}Cu$ value of the paired hydrothermal fluid, indicating that chalcopyrite in the inner ~5 mm of the chimney records the Cu isotope ratio of the venting fluid. Beyond this, an increase in sulfide $\delta^{65}Cu$ toward the exterior correlates with an increase in the relative abundance of secondary Cu sulfides. The appearance of bornite coincides with the presence of small barite crystals, suggesting this represents a redox gradient between reduced hydrothermal fluids and oxidized seawater admixing inwards. Elevated $\delta^{65}Cu$ in this zone can be explained by the precipitation of secondary Cu sulfides from ^{65}Cu-enriched fluids formed during oxidative chalcopyrite dissolution. Our findings indicate that interactions with oxidizing seawater shift chalcopyrite $\delta^{65}Cu$ values over small spatial scales, and that caution must be applied if chimney sulfides are used to reconstruct $\delta^{65}Cu$ values of high-temperature hydrothermal fluids.
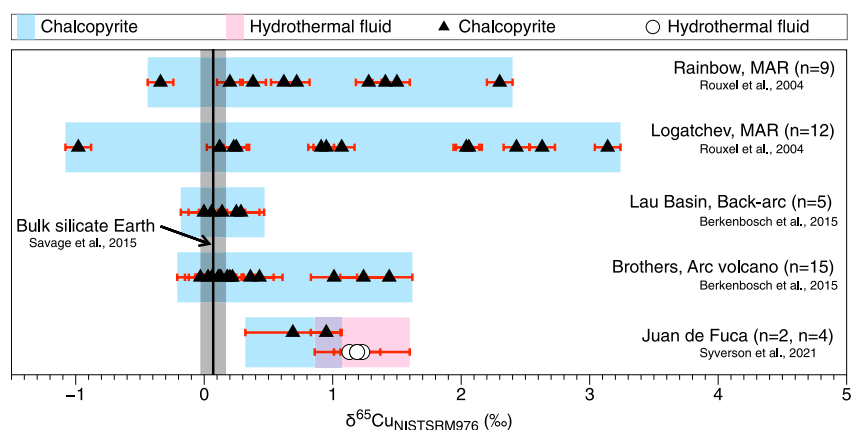
Plain Language Summary Kilometers below the surface of the ocean, hydrothermal "chimney" structures emit hot and metal-rich fluids from the seafloor. The chemical composition of these hot fluids can tell about the reactions that occur beneath the seafloor. In this study, we test how copper-bearing minerals in a hydrothermal chimney record and preserve the copper isotopic composition of these hot fluids. To do so, we compare copper isotope ratios in a hydrothermal fluid and its paired chimney from a seafloor hot spring near Papua New Guinea and find that these ratios are very similar for minerals only in the innermost part of the chimney. Copper isotope ratios increase as the mineralogy of copper changes toward the outside of the chimney wall. This appears to result from cold seawater that enters the chimney and modifies the chemistry and mineralogy of the minerals in the structure. The resulting changes in copper isotope ratios within small cm-scales of the chimney wall are as large as overall ranges observed in copper isotope ratios from seafloor hot springs globally. Therefore, our findings act as a cautionary tale for the use of chimney minerals to reconstruct the copper isotopic composition of hydrothermal fluids.

1. Introduction

Copper isotope ratios ($\delta^{65}Cu$) in hydrothermal fluids have the potential to provide insights into high-temperature reactions between fluids and minerals occurring below the seafloor. For example, experimental work has demonstrated small but measurable isotope effects during precipitation of chalcopyrite ($CuFeS_2$) from hydrothermal fluids (Syverson et al., 2021), and preferential leaching of the light Cu isotope (^{63}Cu) during the dissolution of chalcopyrite under hydrothermal conditions (250–300°C) (Maher et al., 2011). In addition, quantum chemical calculations suggest that copper-chloride complexes formed during phase separation will be depleted in the heavy Cu isotope (^{65}Cu) compared to the vapor phase (Seo et al., 2007; Sherman, 2013). Redox-controlled remobilization of primary Cu sulfide minerals has also been shown to generate large Cu isotope effects

Figure 1. Overview of the copper isotope signatures measured in chalcopyrite and hydrothermal fluids collected in different geological settings, from mid-ocean ridges (MAR = Mid-Atlantic Ridge, Juan de Fuca) to arc and back-arc systems (Lau Basin and Brothers volcano). Data from Berkenbosch et al. (2015), Rouxel et al. (2004), Savage et al. (2015), and Syverson et al. (2021).

in secondary supergene minerals due to preferential oxidative dissolution of ^{65}Cu from chalcopyrite (Gregory & Mathur, 2017; Larson et al., 2003; Mason et al., 2005; Mathur et al., 2009). These findings suggest that Cu isotopes in hydrothermal vent fluids can be used to trace physicochemical processes in the subsurface, from metal leaching in the deepest parts of hydrothermal systems to the precipitation of primary and secondary copper sulfides in the shallow subsurface.

However, accurate quantification of metal abundances and their isotope ratios of high-temperature hydrothermal vent fluids is challenging due to the inherent precipitation of sulfides within sampling devices and the potential for contamination by entrained chimney particles during sampling (Craddock, 2008; John et al., 2008; McDermott et al., 2018; Rouxel et al., 2008). As a result, data constraining the Cu isotope ratios of endmember hydrothermal fluids are scarce (Syverson et al., 2021) and most studies to date have focused on sulfide-rich hydrothermal chimney samples, which show a large range in $\delta^{65}Cu$ values (Figure 1). Zhu et al. (2000) observed a variation of 1.7‰ in chalcopyrite from the East Pacific Rise, Galapagos Rift and Mid-Atlantic Ridge, and Rouxel et al. (2004) reported even larger (~5‰) variations in hydrothermal chimneys from the Lucky Strike, Rainbow and Logatchev vent fields on the Mid Atlantic Ridge. Berkenbosch et al. (2015) reported several per mil $\delta^{65}Cu$ variation (−0.03–1.14‰) within a single chimney at Brothers volcano (Kermadec arc) and interpreted these variations to reflect changes in the vent fluid Cu isotopic composition over short time scales (less than 1 year). However, the large range in $\delta^{65}Cu$ values (−16.48–9.8‰) observed in secondary copper sulfide minerals in land-based ore deposits (Gregory & Mathur, 2017; Larson et al., 2003; Mason et al., 2005; Mathur et al., 2009) questions whether the $\delta^{65}Cu$ variations in seafloor hydrothermal chimneys are of primary origin. Instead, these variations may be the result of Cu isotope fractionation during low-temperature alteration of hydrothermal chimney minerals (Ehrlich et al., 2004; Qi et al., 2019) or reworking of altered primary copper sulfides by high-temperature fluids (Rouxel et al., 2004). This would complicate the use of hydrothermal chimneys in reconstructing high-temperature fluid $\delta^{65}Cu$ values.

In this study, we therefore examine the extent to which chalcopyrite-rich hydrothermal chimney records the primary fluid $\delta^{65}Cu$ value, using a fluid-chimney pair from the Roman Ruins vent field in the PACMANUS area of Manus Basin. We reconstruct the hydrothermal fluid $\delta^{65}Cu$ from Cu isotope analyses of dissolved and precipitated phases in the fluid sampler and compare this value with sulfide $\delta^{65}Cu$ in two microdrilled transects across the chimney wall. Cu isotope variations are examined against mineralogical and geochemical data as well as sulfide sulfur isotope ratios ($\delta^{34}S$) to constrain the processes responsible for the preservation and alteration of fluid $\delta^{65}Cu$ in hydrothermal chimneys.

2. Sample Collection

Samples for this study were collected from the Roman Ruins vent area at the PACMANUS vent field, a large felsic-hosted hydrothermal system located in the Manus Basin, northeast of Papua New Guinea (Figure 2) (Binns & Parr, 1993; Taylor, 1979). Venting at PACMANUS occurs at multiple discrete vent areas that are
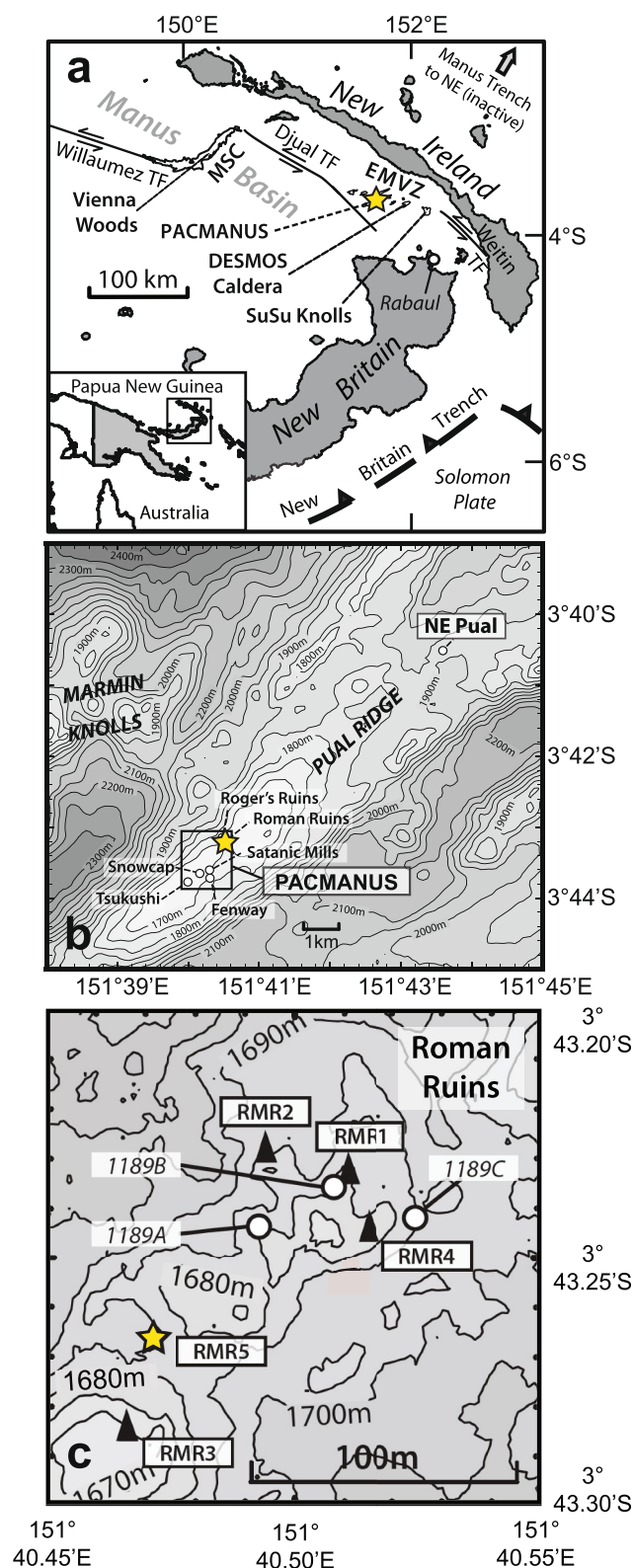
Figure 2. Maps showing the location of the studied hydrothermal chimney. (a) Overview map showing the main vent field areas in the Eastern Manus back-arc Basin and the location of PACMANUS (yellow star). (b) Map of the PACMANUS vent field with the location of Roman Ruins (yellow start). (c) Detailed map of the sampling location of chimney RMR5 (yellow star) compared to locations of high temperature fluid samples from 2006. Adapted from Reeves et al. (2011, 2014).

dispersed along a ∼2 km section of the neovolcanic crest of Pual Ridge, including Roman Ruins and Roger Ruins to the northeast, and Fenway, Satanic Mills and Solwara-8 to the south (Thal et al., 2014). Roman Ruins, at 1,639–1,774 m depth, is the largest of these areas at ∼150 m in diameter (Beaudoin et al., 2007; Thal et al., 2014; Wilckens et al., 2018) (Figure 2). Active vents at Roman Ruins are found in the southwestern part, where sulfide chimneys vigorously vent fluids up to 341°C (Reeves et al., 2011). The fluids are characterized by low $pH_{(25°C)}$ values (2.3–2.6) and elevated metal concentrations in comparison to most mid-ocean ridge fluids (Humphris & Klein, 2018; Reeves et al., 2011).

During the 2011 expedition SO-216 with R/V *Sonne* (Bach & Participants c, 2011), a large (∼1 m in length) actively venting hydrothermal chimney structure (RMR5) with a wide central conduit and several smaller chimney spires located atop its bulbous head was collected from the Roman Ruins area using the ROV *QUEST* (Figure 3). Prior to recovering the main conduit, one of these spires was removed for better access and samples of the associated vent fluid were taken from an orifice emanating from the central conduit (Reeves et al., 2014). Duplicate samples of the hydrothermal fluid were obtained using Isobaric Gas Tight (IGT) samplers (Seewald et al., 2002), and geochemical and isotopic compositions from these samples have previously been reported by Reeves et al. (2014) and Wilckens et al. (2018). The maximum temperature measured during fluid collection (333°C; Table 1) was not stable and both IGT samplers experienced some degree of seawater entrainment due to deployment difficulties; 333°C must therefore be viewed as a minimum temperature estimate.

3. Methods

3.1. Sample Preparation

Upon recovery to shore, the entire RMR5 central chimney conduit and top section was stored in a sealed container under nitrogen atmosphere until further processing to avoid oxidation of sulfide minerals. The chimney was subsequently cut using a diamond-blade saw and a thick section was made from one subsample (Figure 3). Mineralogical variations in the thick section were mapped as backscattered-electron (BSE) image greyscale values using a Zeiss Supra 55 VP scanning electron microscope (SEM) at the ELMILAB of the University of Bergen, producing a total of 570 image tiles. A map was generated using the Grid/Collection stitching plugin in the FIJI (ImageJ) software (Preibisch et al., 2009; Schneider et al., 2012). Micro-scale chemical compositions were determined using a JEOL JXA 8200 Superprobe electron microprobe at the Freie Universität Berlin, and pixel greyscale counting was used to determine relative number of minerals and porosity in the sample. The thick section was subsequently microdrilled along two transects using a New Wave Research MicroMill equipped with a 0.27 mm diameter tungsten-carbide drill bit. Resulting sample powders (0.05–1.2 mg) were digested in aqua regia for geochemical and isotope analyses.

Hydrothermal fluid samples from the Roman Ruins vent were processed within 12 hr after shipboard recovery following methods outlined in Reeves

et al. ([2011](#)) and Craddock ([2009](#)). For metal analyses, a 30 ml aliquot of each fluid sample was acidified immediately at sea to pH < 2 with 200 μL concentrated distilled HNO_3, comprising what is known as the "dissolved" fraction. Cu, like other transition metals, readily precipitates upon cooling (Trefry et al., [1994](#)) both in the IGT samplers and during subsequent storage, additionally forming what is known as a particulate "dregs" fraction. Some small precipitates also form during the storage of the acidified fluid aliquots, termed the "bottle-filter" fraction. It is therefore necessary to quantitatively collect, re-digest and analyze these particles to reconstitute the original fluid Cu content accurately (Craddock, [2009](#); McDermott et al., [2018](#)). The sampler dreg fractions were recovered onto 0.22 μm nylon membrane filters from the IGT samplers at sea, while the bottle filter fractions were recovered using the same filter type onshore using PE/PP syringes and filter holders. Both particulate fractions were separated from their filters and redigested using ∼5 mL of reverse *aqua regia* (∼1:3 $HCl:HNO_3$) in a 30 mL Savillex^{TM} beaker at 70–80°C overnight until the particles dissolved and the solution evaporated to near dryness (Craddock, [2009](#); McDermott et al., [2018](#)). This digestion and dry-down process was repeated twice with trace metal grade HNO_3 alone to remove chloride and ensure complete digestion as possible. Digested residues of both the dregs and bottle filter fractions were then re-dissolved in 3N HNO_3 prior to ICP-MS analyses.

3.2. Geochemical Analyses

Major cations (Na^+, Ca^{2+}, K^+) and anions (Cl^-, SO_4^{2-}) in Table [1](#) were determined by ICP-OES and ion chromatography, respectively, at the University of Bremen. Dissolved gases (CO_2, H_2, H_2S) were determined as outlined in Reeves et al. ([2011](#)) either at sea or onshore in Bremen. Analytical uncertainties on analyses of the cations, anions and gases are ≤5% (2s). Cu, Zn, and Fe concentrations in the various fractions were determined by inductively-coupled plasma mass spectrometry (ICP-MS) using a Thermo Scientific Element XR at the University of Bergen, following the approach of McDermott et al. ([2018](#)). The three fluid fractions were mathematically combined to reconstitute the original fluid sample Cu, Zn, and Fe concentrations, with an estimated analytical uncertainty of ±10% (2s). As the fluid samples represent a two-component mixture between an endmember hydrothermal fluid (assumed to be near zero Mg, Reeves et al., [2011](#)) and seawater (52.4 mM Mg) entrained during sampling, the endmember Cu, Zn, and Fe concentrations were determined by extrapolating measured concentrations to zero Mg with linear regression forced through seawater composition (assumed to be zero for these metals) (Von Damm et al., [1985](#)). Digested chimney powders were analyzed for concentrations of Ba, Ca, Cu, Fe, S, and Zn using ICP-MS (Thermo Scientific Element XR) at the Pole Spéctroscopie Océan (PSO) of IFREMER, with an average analytical uncertainty of ±10% (2s).

3.3. Copper Isotope Analyses

Aliquots of the dissolved micro-drilled powders and each one of the fluid fractions were prepared for Cu isotope analyses following the method of Dekov et al. ([2016](#)). Solutions were evaporated to dryness, redissolved in 6M HCl, and purified through an anion-exchange chromatographic column filled with 2 mL (wet volume) of Bio-Rad AG-MP1 resin (Borrok et al., [2007](#); Maréchal et al., [1999](#)). Because Cu concentrations in the dissolved fractions were too low for Cu isotope analyses, dissolved and bottle-filter fractions were recombined at a 1:1 ratio before column purification procedures. In addition, samples with seawater matrices were purified twice on the anion exchange column to ensure the removal of Ca^{2+} and Na^{+}, which could otherwise lead to isobaric interferences from $^{23}Na^{40}Ar^+$ on ^{63}Cu (May & Wiedmeyer, [1998](#)). The dissolved powders were purified only once on the anion-exchange column.

Copper isotope analyses were performed at the PSO (IFREMER) on a Thermo Fisher Neptune multi-collector inductively coupled plasma mass spectrometer (MC-ICP-MS) in low resolution mode. Samples containing 200 ppb Cu were introduced into the instrument using a microconcentric PFA nebulizer and cyclonic spray chamber as better signal stability is obtained in a wet plasma mode (Baconnais et al., [2019](#)). Mass bias was corrected by standard-sample bracketing and copper isotope ratios were calculated following the equation:

$$\delta^{65}Cu = \left(\frac{R_{sample}}{R_{standard}} - 1\right) \times 1000\ (\permil)$$

where R_{sample} is the $^{65}Cu/^{63}Cu$ ratio of the sample and $R_{standard}$ is the $^{65}Cu/^{63}Cu$ ratio of the NIST-SRM 976 standard measured before and after each sample. The precision during the analytical sessions was 0.02‰ (2sd)
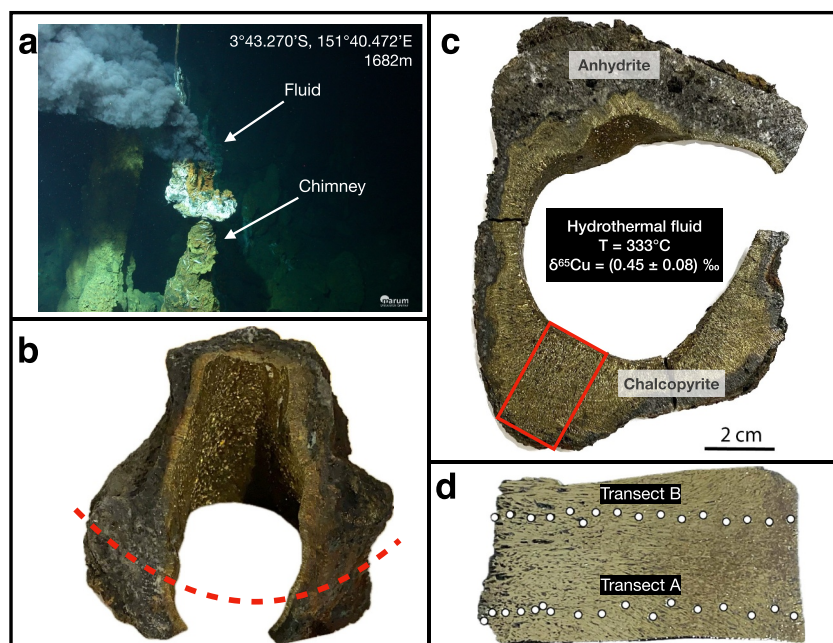
Figure 3. Overview of the chimney investigated in this study. (a) Photographs at the seafloor adapted from Reeves et al. (2014) of chimney RMR5. (b) Chimney sample with the slice cut indicated by the red dashed line. (c) Cross-section of the chalcopyrite-rich chimney wall with the composition and measured temperature of the paired fluid indicated, red box indicates the area selected for the thick section. (d) Overview of the thick section with micro-drilled spot locations on transects A and B, with the inside wall on the left and the exterior on the right.

based on repeated analyses ($n = 245$) of NIST-SRM 976 over 3 days. The analysis of multiple purifications of a multi-element synthetic standard yielded a precision of 0.04‰ (2sd, $n = 12$). Column yields higher than 97% confirm the quantitative recovery of all copper during anion-exchange chromatography and, therefore, no copper isotope fractionation during sample purification (Maréchal & Albarède, 2002). Fluid δ^{65}Cu values were calculated from the δ^{65}Cu obtained for each fraction and their relative contributions to the total copper content of the fluid. As such, the δ^{65}Cu of the fluid generally corresponds to the dregs δ^{65}Cu.

3.4. Sulfur Isotope Analyses

Cu isotope analyses of microdrilled chimney powders were complemented with S isotope analyses (δ^{34}S) to characterize the source of sulfur for the sulfide minerals. Aliquots of the dissolved powders were purified prior to isotope analysis using columns filled with 1.8 mL (wet volume) of Bio-Rad AG50-X8 cation exchange chromatographic resin (Craddock, 2009). Samples were loaded onto the resin in 1 mL 2% HNO_3, and S was eluted in 5 mL 2% HNO_3. Yields were 99% or higher for all samples. The final solutions were diluted to concentrations between 1 and 10 ppm S, and analyzed in a series of samples and a SPEX standard solution with matching S concentrations.

Sulfur isotopes were measured at the PSO (IFREMER) on a Thermo Fisher Neptune multi-collector inductively coupled plasma mass spectrometer in medium-resolution mode using a microconcentric PFA nebulizer and cyclonic spray chamber. Mass bias was corrected using standard-sample bracketing (Albarede, 2004; Belshaw et al., 1998; Craddock, 2009), with the ^{34}S/^{32}S ratio measured for each sample being normalized to the ^{34}S/^{32}S of a SPEX standard measured before and after the sample. Sulfur isotope ratios are determined using the equation:

$$\delta^{34}S = \left(\frac{R_{\text{sample}}}{R_{\text{standard}}} - 1 \right) \times 1000 \ (‰)$$

Data are normalized to the international standard V-CDT using a SPEX standard δ^{34}S value of 3.5‰ versus V-CDT. The precision is calculated on repeated analysis of a SPEX standard for each S concentration series and

Table 1
Measured and Calculated Concentrations of Dissolved Elements, Gases and Reconstituted Metals in Duplicate IGT Samples of the RMR5 Vent Fluid (T_{max} = 333°C)

Sample (cruise ID)	Fluid fraction (for Fe, Cu, Zn)	Mg (mm)	$pH_{(25°C)}$[a]	Na (mm)	Cl[a] (mm)	Ca (mm)	K (mm)	Cu (μm)	Zn (μm)	Fe (mm)	H_2S[a] (mM)	H_2[a] (μM)	ΣCO_2[a] (mm)	SO_4^{2-} (mM)	$\delta^{65}Cu_{SRM987}$ (‰)	±2s (‰)	Cu in fraction (%)
S039-IGT3 (039-ROV-02)	Reconstituted	20.3	3.3	538	656	18.7	59	115	94	4.16	1.9	12.3	12	10.8	0.48	0.04	100
	B/F + Dissolved														0.50	0.08	
	B/F							0.7	1.8	0.14							0.6
	Dissolved							16	58	3.70							13.6
	Dregs							98.7	34	0.311					0.47	0.04	85.9
S039-IGT7 (039-ROV-03)	Reconstituted	5.3	2.6	571	716	22.3	81	177	177	5.94	3.4	22.4	18	2.0	0.42	0.04	100
	B/F + Dissolved														0.36	0.08	
	B/F							0.6	1.9	0.086							0.4
	Dissolved							38	139	5.41							21.1
	Dregs							139	36	0.436					0.44	0.04	78.5
RMR5$_{EM}$ (333°C) Endmember		0	2.6*	578	733	23.6	89	193	182	6.63	3.5	23	19	–	0.45	0.04	

Note. T_{max} = maximum-measured temperature at vent; *lowest measured $pH_{(25°C)}$ is assumed to approximate the endmember $pH_{(25°C)}$ (after Reeves et al. (2011)); mM, mmol/L fluid; mm, mmol/kg fluid; μM, μmol/L fluid; μm, μmol/kg fluid. [a]Data previously reported by Reeves et al. (2014) and Wilckens et al. (2018).
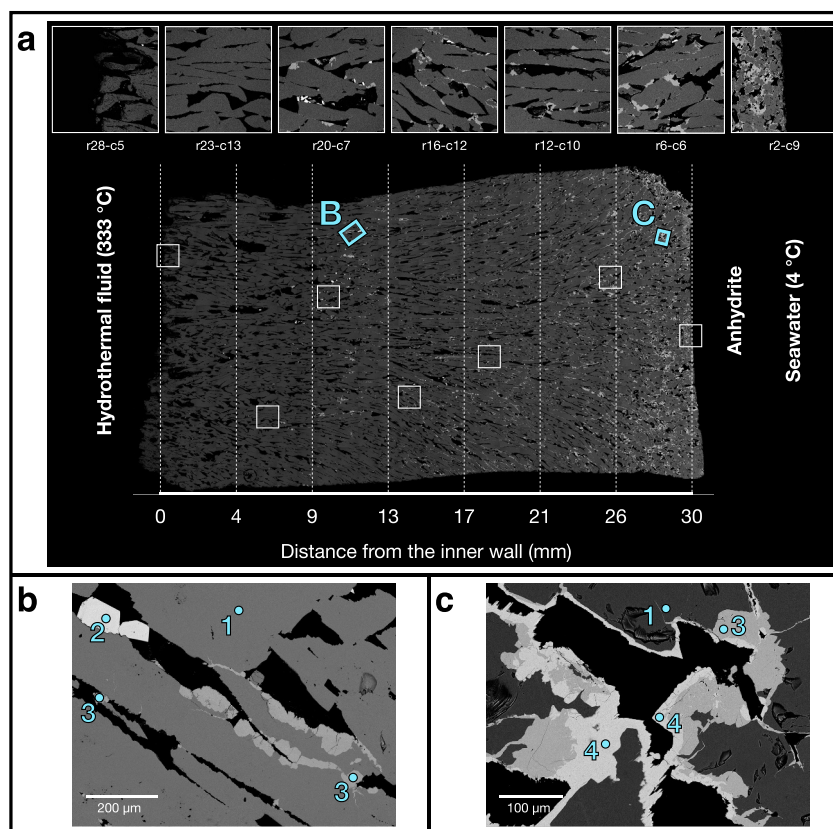
Figure 4. Backscattered electron maps of the chimney wall section displaying mineralogical variations. (a) Overview image composed of 570 tiles, with a selection of tiles shown separately (r = row number, c = column number). (b) Detail image of area B in Zone 3, and (c) Detail image of area C in Zone 4. Mineral phases are identified as 1 = chalcopyrite, 2 = barite, 3 = bornite, 4 = chalcocite (see Supporting Information S1).

ranges from 0.06 to 0.54‰. Analyses of a multi-element synthetic standard yielded a precision of 0.11‰ (2sd, n = 4).

3.5. Computational Methods

The chemical composition of bulk samples retrieved by microdrilling was used to compute mineral modes for comparison with mineral abundance estimates from SEM images. The abundances of barite ($BaSO_4$), anhydrite ($CaSO_4$), and sphalerite (ZnS) were calculated from Ba, Ca, and Zn concentrations, respectively. Using measured Cu and Fe concentrations and the sulfide concentration corrected for sphalerite, the abundances of chalcopyrite ($CuFeS_2$), bornite (Cu_5FeS_4), and chalcocite (CuS_2) were determined by least-squares mass balancing. In addition, a thermodynamic reaction path model was computed with Geochemist's Workbench Version 12 using a tailor-made 25 MPa database and assuming mixing of the endmember RMR5 hydrothermal vent fluid composition (Table 1) with seawater in a 1:15 mass ratio as temperature drops from 333°C to 5°C.

4. Results

4.1. Chimney Mineralogy

Backscattered-electron imaging and electron microprobe analyses (Supporting Information S1) show that the mineralogy of the studied thick section is dominated by chalcopyrite (95.1%) with minor secondary copper sulfides (4.3%) and barite (0.5%) (Figure 4). The relative abundance of these mineral phases varies throughout the thick section. Secondary copper sulfides and barite are absent in the innermost part (0–4 mm) of the wall (Zone 1), but small barite grains appear between 4 and 9 mm (Zone 2). Rims of secondary copper sulfides on chalcopyrite appear at 9 mm (Figure 4a) and gradually increase in abundance toward the outer part of the chimney wall (Zone 3). Based on electron microprobe analyses, bornite ($Cu_{4.7}Fe_{1.1}S_4$) is the dominant secondary copper sulfide in this zone.

However, in the outermost part of the chimney wall (26–30 mm), rims are observed on bornite with a higher BSE brightness (Figure 4b), and microprobe data indicate that this most likely represents chalcocite (Zone 4).

Calculated estimates on the abundance of chalcopyrite in micro-drilled powder range from 79 to 100 wt.% in transect A, and 82–94 wt.% in transect B (Table 2). The abundance of chalcopyrite was anticorrelated with the modeled abundance of bornite and chalcocite in both transects (Figure 5). In transect A, bornite abundance varies between 2.5 and 6.6 wt.% in Zones 1, 2, and 3, and increases to 9.0 wt.% in Zone 4. Similarly, the computed chalcocite abundance is relatively stable at 1.1–3.8 wt.% in Zones 1 and 2, but increases to 7.5 wt.% in Zone 3 and further to 11.2 wt.% in Zone 4. In transect B, the abundance of bornite in Zones 1, 2, and 3 is higher than in transect A and ranges from 4.9 to 7.6 wt.%, with an increase to 8.3 wt.% in Zone 4. Similar to transect A, the abundance of chalcocite ranges from 1.1 to 3.5 wt.% in Zones 1 and 2, and increases to 8.1% in Zone 3% and 9.7% in Zone 4.

The presence of chalcopyrite, bornite and chalcocite in the chimney is also predicted from the reaction path model computation built using the RMR5 hydrothermal fluid end member composition (Figure 6). Calculated changes in the saturation states of Cu-(Fe)-S phases with decreasing temperature suggest precipitation of chalcopyrite at 310°C, followed by bornite at 270°C and chalcocite at 220°C.

4.2. Hydrothermal Fluid Composition

The duplicate RMR5 hydrothermal fluid samples (333°C, $pH_{25°C} = 2.6$) plotted on a consistent linear regression trend with dissolved Mg (Figure 7), indicating highly conservative behavior of the reconstituted sample Cu concentrations and providing no indication of significant particle loss or gain during sampling or processing. The RMR5 (333°C) endmember Cu concentration (193 ± 19 µmol/kg) calculated (Table 1) is also within error of the 2006 endmember Cu concentration previously reported for the "RMR4" vent (341°C) at the Roman Ruins site, which had a similar pH (Figure 1; Craddock, 2009; Reeves et al., 2011). Cu isotope analyses of both RMR5 fluid samples yielded very similar reconstituted $\delta^{65}Cu$ values of 0.48 ± 0.04‰ and 0.42 ± 0.04‰ (Table 1).

4.3. Chimney Isotopic Composition

Measured $\delta^{65}Cu$ values in the micro-drilled powders from the transect A range from 0.46 to 2.21‰, with the lowest values found in the innermost part of the chimney (0.8 mm). Copper isotope ratios increase with increasing distance to the chimney conduit, with $\delta^{65}Cu$ values of 0.46–0.62‰ in Zone 1, 1.11–1.42‰ in Zone 2, 1.75–2.18‰ in Zone 3, and 1.27–2.21‰ in Zone 4. A similar trend is observed in transect B, where the overall $\delta^{65}Cu$ values range from 0.30 to 2.28‰ and the lowest $\delta^{65}Cu$ is measured in Zone 1 (0.30–0.58‰), compared to 0.97–1.22‰ in Zone 2, 1.17–2.28‰ in Zone 3 and 1.58–1.63‰ in Zone 4 (Table 2). Values measured in chalcopyrite from the conduit lining (0.47 and 0.58‰) are similar to the copper isotopic composition measured in the paired hydrothermal fluid (333°C) with $\delta^{65}Cu = 0.48‰$ (Table 1).

Associated sulfur isotope ratios ($\delta^{34}S$) in the transect A fall between 1.52 and 4.72‰, with an average value of 2.85‰ (Figure 7). Measured $\delta^{34}S$ values increase from 1.52 to 3.14‰ in Zone 1, stabilize between 2.31 and 3.46‰ in Zones 2 and 3, except for a high value of 4.72‰ at 14 mm, and decrease in Zone 4 from 4.01 to 2.04‰ (Table 2). Transect B displays a similar trend where sulfur isotope ratios range from 2.36 to 3.74‰, with the maximum $\delta^{34}S$ value measured at 14 mm distance from the chimney conduit (Table 2).

5. Discussion

5.1. Record of Fluid $\delta^{65}Cu$ in Conduit Chalcopyrite

The Cu isotopic composition of the hydrothermal fluid at Roman Ruins ($\delta^{65}Cu = 0.45 ± 0.08‰$) is within the error of the composition of chalcopyrite in the inner wall of the chimney ($\delta^{65}Cu = 0.47 ± 0.04‰–0.58 ± 0.06‰$). Given the generally well-conserved nature of the reconstituted dissolved Cu concentrations (Figure 7), it is highly unlikely that this similarity reflects the contamination of the dregs fractions with Cu-rich particles from the chimney interior during sampling, which would have produced a poor Cu concentration correlation with Mg. We also exclude the possibility that our fluid $\delta^{65}Cu$ value results from Cu isotope fractionation in the IGT samplers during cooling, as we analyzed both the dissolved and precipitated copper in the sampler and $\delta^{65}Cu$ values for both fractions were indistinguishable from each other (Table 1). For both analyzed fluids, the majority of all Cu was present in the dregs fraction (78.5%–85.9%), in agreement with the low solubility of copper sulfides below

Table 2
Copper and Sulfur Isotope Composition and Mineralogy of the Micro Drilled Powders Along the Two Transects

Name	Distance from inside wall (mm)	$\delta^{65}Cu_{SRM987}$ (‰)	2sd (‰)	$\delta^{34}S_{VCDT}$ (‰)	2sd (‰)	Cu (wt %)	Fe (wt %)	S (wt %)	Zn (wt %)	Ba (wt %)	Ca (wt %)	Fe/Cu (molar ratio)	S/Cu (molar ratio)	Chalcopyrite (wt%)	Bornite (wt%)	Chalocite (wt%)	Sphalerite (wt%)	Barite (wt%)	Comments
Transect A																			
Lining	0.0	0.47	0.04	1.52	0.54	34	27	31	−1.0	0.0	8.0	0.9	1.8	69	2.4	1.7	0.0	0.0	
Lining chip	0.0	0.64	0.04	2.25	0.41	37	29	34	0.0	0.0	0.5	0.9	1.8	92	3.7	3.0	0.1	0.0	
A1	0.8	0.46	0.04	2.74	0.41	38	29	34	0.1	0.0	−0.6	0.9	1.8	92	4.2	3.7	0.2	0.1	
A2	2.1	0.54	0.04	2.42	0.42	37	29	35	0.9	0.0	−2.6	0.9	1.9	93	3.1	2.1	1.3	0.0	
A3	3.6	0.62	0.04	3.14	0.11	36	28	37	−0.5	0.1	−2.1	0.9	2.1	97	2.5	1.1	0.0	0.1	
A4	5.0	1.11	0.04	2.31	0.54	37	27	34	0.4	0.1	1.0	0.8	1.8	88	4.1	3.7	0.7	0.2	
A5	5.8	1.15	0.10	3.12	0.38	34	31	34	0.1	0.0	0.0	1.0	2.0	100	0.0	0.0	0.2	0.0	
A6	6.5	1.37	0.06	2.82	0.38	35	28	35	1.8	0.0	0.6	0.9	2.0	91	2.9	1.9	2.7	0.0	
A7	9.2	1.42	0.04	3.09	0.41	35	28	34	0.0	2.1	0.1	0.9	1.9	91	3.1	2.2	0.0	3.5	
A8	11.5	2.08	0.04	2.75	0.41	33	24	30	1.7	0.0	11.2	0.8	1.8	54	2.8	2.7	2.6	0.0	
A9	13.8	2.18	0.05	4.72	0.26	35	27	35	0.0	0.2	2.8	0.9	2.0	86	2.7	1.7	0.0	0.4	
A10	16.5	1.81	0.04	2.90	0.26	38	27	34	−0.1	0.1	0.1	0.8	1.8	90	5.0	4.9	0.0	0.2	
A11	18.3	1.75	0.04	3.36	0.26	38	27	34	0.0	0.2	1.7	0.8	1.8	84	4.9	5.0	0.0	0.3	
A12	20.9	1.84	0.04	2.80	0.60	39	26	33	0.5	0.3	0.9	0.8	1.7	82	6.3	7.2	0.8	0.6	
A13	23.4	2.05	0.04	3.46	0.26	35	25	32	1.8	0.1	6.7	0.8	1.8	67	3.8	3.9	2.6	0.1	
A14	26.2	1.88	0.09	4.01	0.38	38	23	31	0.1	0.5	7.6	0.7	1.6	61	5.7	6.9	0.1	0.9	
A15	28.4	1.27	0.04	2.61	0.38	43	27	32	−0.2	0.0	−1.8	0.7	1.4	80	9.0	11.3	0.0	0.0	
A16	30.3	2.21	0.04	2.04	0.32	41	25	31	0.7	0.0	1.6	0.7	1.5	75	8.3	10.4	1.1	0.0	
Transect B																			
B1	0.0	0.58	0.06	2.40	0.60	36	28	33	−0.5	0.0	3.6	0.9	1.8	82	4.6	1.7	0.0	0.1	
B2	1.5	0.54	0.04	2.36	0.40	37	30	34	−0.1	0.0	−1.1	0.9	1.8	93	5.2	1.8	0.0	0.0	
B3	3.5	0.30	0.04	2.98	0.54	37	28	35	−0.2	0.1	0.7	0.9	1.9	90	5.2	2.1	0.0	0.2	
B4	5.5	1.08	0.04	2.85	0.26	37	29	34	0.1	0.0	0.1	0.9	1.8	94	4.9	1.1	0.1	0.0	
B5	7.4	0.97	0.10	2.54	0.41	37	28	33	0.4	0.0	0.7	0.9	1.8	89	5.3	2.4	0.5	0.0	
B6	8.6	1.22	0.04	2.51	0.26	38	28	34	0.1	0.3	−0.3	0.9	1.8	90	5.8	3.5	0.2	0.5	
B7	9.9	1.17	0.04	2.44	0.26	40	29	34	−0.6	0.0	−1.9	0.8	1.7	89	6.3	4.6	0.0	0.0	
B8	12.0	1.34	0.04	2.66	0.43	38	29	34	−0.1	0.8	−2.1	0.9	1.8	91	5.2	2.1	0.0	1.3	
B9	14.1	1.84	0.04	3.74	0.26	36	28	34	0.0	0.0	1.9	0.9	1.9	87	4.9	1.8	0.0	0.0	
B10	16.2	1.68	0.04	2.53	0.41	39	28	33	−0.2	0.0	0.0	0.8	1.7	89	6.2	4.5	0.0	0.0	
B11	18.3	1.73	0.04	2.68	0.41	39	27	34	−0.2	0.0	0.0	0.8	1.7	88	6.5	5.3	0.0	0.0	
B12	20.4	2.05	0.04	3.18	0.41	37	27	33	0.4	0.3	3.0	0.8	1.8	79	5.5	3.9	0.6	0.5	

Table 2
Continued

| Name	Distance from inside wall (mm)	$\delta^{65}Cu_{SRM987}$ (‰)	2sd (‰)	$\delta^{34}S_{VCDT}$ (‰)	2sd (‰)	Cu (wt%)	Fe (wt%)	S (wt%)	Zn (wt%)	Ba (wt%)	Ca (wt%)	Fe/Cu (molar ratio)	S/Cu (molar ratio)	Chalcopyrite (wt%)	Bornite (wt%)	Chalocite (wt%)	Sphalerite (wt%)	Barite (wt%)	Comments
B13	22.6	1.91	0.04	3.39	0.41	38	26	33	0.2	0.0	3.0	0.8	1.7	77	6.5	6.3	0.4	0.1	
B14	24.7	2.28	0.04	3.29	0.41	40	25	34	−0.4	0.0	0.8	0.7	1.7	82	7.4	7.8	0.0	0.1	
B15	26.8	1.63	0.05	2.63	0.40	37	33	31	0.1	0.1	−1.0	1.0	1.6	94	5.3	0.0	0.1	0.1	Iron oxide
B16	28.9	1.58	0.04	2.56	0.26	41	27	31	0.6	0.1	0.2	0.7	1.5	80	8.1	9.5	0.8	0.2	
Average		1.38	0.59	1.58	1.20														

Note. mm, millimeters.
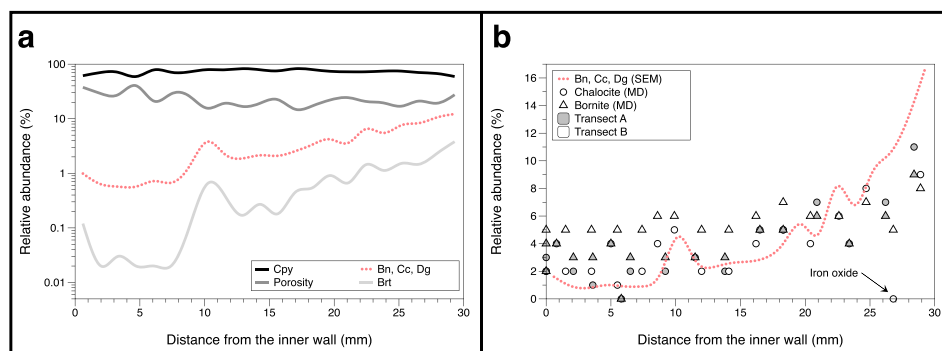
Figure 5. Relative mineral abundances through the chimney wall. (a) Relative abundances of chalcopyrite (Cpy, black line), porosity (gray line), secondary copper phases (Bn: bornite, Cc: chalcocite, Dg: digenite, red dotted line) and barite (Brt, light gray line) as determined by pixel counting on SEM images along transect B. (b) Comparison between relative abundances of secondary copper phases determined by SEM (red dotted line) and relative abundances of chalcocite (circles) and bornite (triangles) along transect A (gray) and transect B (white) calculated from the chemical composition of the microdrilled powders.

250°C (Crerar & Barnes, 1976), and other studies using similar hydrothermal fluid metal reconstitution procedures (McDermott et al., 2018; Syverson et al., 2021).

The similarity between the δ^{65}Cu values of the hydrothermal fluid and chalcopyrite in Zone 1 indicates that Cu isotope fractionation is limited during sulfide precipitation. This is consistent with the experimentally determined equilibrium fractionation factor between chalcopyrite and dissolved Cu^{2+} at 350°C of $-0.22 \pm 0.16\permil$ (Syverson et al., 2021). However, the subhedral to anhedral nature of the chalcopyrite crystals observed in our thick section (Figure 4) as well as the large amount of time required to establish Cu isotopic equilibrium ($\sim$1,000 hr, Syverson et al., 2021) suggests that Cu isotopic equilibrium may not have been established in the studied chimney. However, regardless of whether the observed lack of Cu isotope fractionation between the hydrothermal fluid and chalcopyrite reflects isotopic equilibrium or not, our findings indicate that chalcopyrite in the innermost ($\sim$5 mm) wall of the chimney records the δ^{65}Cu value of the hydrothermal fluid. This implies that fluid δ^{65}Cu values can be reconstructed from chimney chalcopyrite, which is generally easier to sample and process for Cu isotope analyses due to the absence of a seawater matrix. It remains unclear whether this conclusion also applies to other sulfide phases that are common in hydrothermal chimneys, such as sphalerite, pyrite, or pyrrhotite. Dekov et al. (2016) reported δ^{65}Cu values of -0.07 and $-0.15\permil$ for enargite (Cu_3AsS_4) from the conduit lining of a hydrothermal
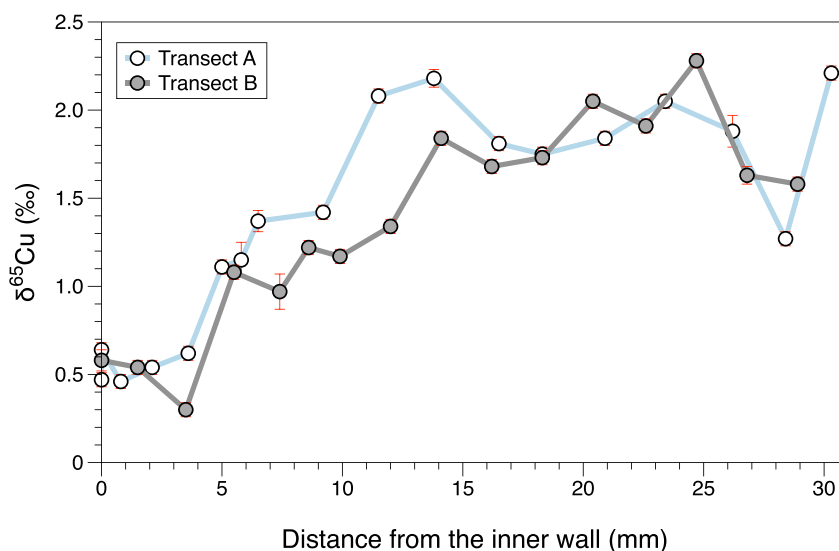
Figure 6. Copper isotope ratios measured in microdrilled chimney powders for transect A and transect B. Error bars (2σ) are displayed in red.
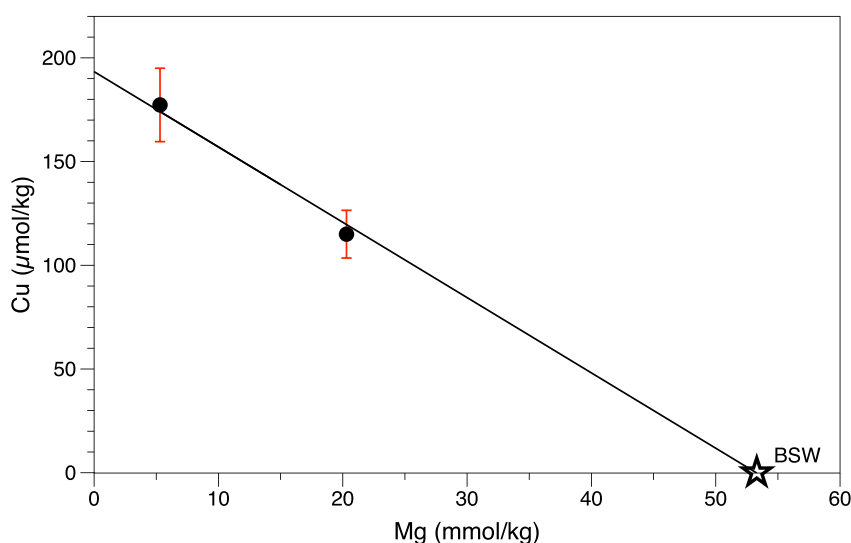
Figure 7. Dissolved Cu concentrations (reconstituted) versus dissolved Mg in duplicate samples of the RMR5 hydrothermal fluid. Star indicates the composition of the bottom seawater (BSW) (52.4 mmol/kg; Reeves et al., 2011; Wilckens et al., 2018) through which the linear regression (solid line) of both samples is forced. BSW Cu is assumed to be 0 μmol/kg for the purpose of regression.

chimney in the North Su venting area at SuSu Knolls (Manus Basin), which are significantly lower than the fluid $\delta^{65}Cu$ value found in our study. Although we cannot exclude the possibility that fluids at North Su have a distinct Cu isotopic composition from those at Roman Ruins, the low $\delta^{65}Cu$ values in the enargite suggest that fractionation may occur during the precipitation of copper-bearing sulfide minerals other than chalcopyrite.

5.2. Changing Sulfide $\delta^{65}Cu$ Throughout the Chimney Wall

In contrast to the innermost chimney wall (Zone 1), Cu isotope ratios increase from fluid-like $\delta^{65}Cu$-values to more ^{65}Cu-enriched ratios ($\delta^{65}Cu \sim 2‰$) in Zones 2, 3, and 4 in both transects (Figure 6). One possible explanation for this variation is that the Cu isotopic composition of the hydrothermal fluid has changed through time, for example, due to changes in subsurface processes such as mineral precipitation or magmatic inputs (cf. Berkenbosch et al., 2015). Although changing source reactions have previously been used to interpret variations in chimney $\delta^{34}S$ values (Shanks et al., 1995; Woodruff & Shanks, 1988), we argue below that this interpretation is unlikely to explain the Cu isotope variations. Back-arc hydrothermal systems can be subject to temporal changes in the magmatic degassing of SO_2, which can impact the abundance and isotopic composition of sulfur in the circulating vent fluids (Gamo et al., 1997; Reeves et al., 2011; Seewald et al., 2015). However, our chimney sulfur isotope data show a relatively limited variation in $\delta^{34}S$ (Figure 8), except for a few elevated $\delta^{34}S$ values in transect A that may be related to the dissolution of sulfate phases with seawater-like $\delta^{34}S$-values ($21.0 \pm 0.02‰$, Rees et al., 1978). Furthermore, our chimney wall average $\delta^{34}S$ value ($2.85‰$, Figure 8) lies within previously reported chalcopyrite lining $\delta^{34}S$ values for the Roman Ruins RMR1, RMR3, and RMR4 vents sampled in 2006 (Figure 1; McDermott et al., 2015), arguing against major temporal changes in fluid sulfur isotope ratios. Although relatively constant sulfur isotope ratios across the wall do not directly imply that copper source reactions remained the same, they do nonetheless reflect general stability of the hydrothermal system with limited changes in sulfide source composition during the growth of the RMR5 chimney. Coupled with the similarity of endmember Cu concentrations in the Roman Ruins area from 2006 to 2011 (noted above), these observations are inconsistent with significant changes in fluid Cu isotope signatures through time.

Instead, we propose that the change in sulfide $\delta^{65}Cu$ values across the chimney wall results from oxidative dissolution of chalcopyrite and re-precipitation of secondary copper sulfide minerals. Previous work indicates that the formation of secondary copper sulfides from chalcopyrite is associated with ^{65}Cu enrichment in dissolved Cu (II) (Mathur et al., 2018; Rouxel et al., 2004; Sherman, 2013), and large Cu isotope variations ($-16.48–9.8‰$) are found in association with supergene deposits that form as a result of oxidative remobilization of primary copper sulfide minerals (Mathur et al., 2005, 2009). Indeed, in our chimney, we observe that the appearance of bornite at a
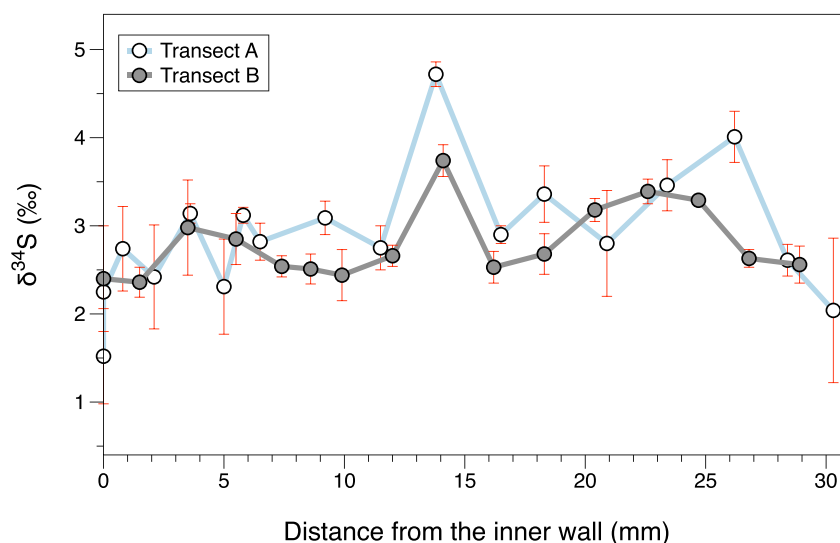
Figure 8. Sulfur isotope ratios measured in microdrilled chimney powders for transect A and transect B. Error bars (2σ) are displayed in red.

distance of ∼9 mm from the innermost wall (Zone 3, Figure 4a) and chalcocite in the outermost wall (Zone 4, Figure 4b) coincide with higher $\delta^{65}Cu$ values measured in this part of the chimney (Figure 6). Bornite and chalcocite both occur as replacement textures on chalcopyrite (Figures 4a and 4b; Supporting Information S1), consistent with the formation of these minerals through the alteration of chalcopyrite. Oxidative dissolution and re-precipitation of chalcopyrite in the chimney is also consistent with the appearance of small-scale (200 μm) sub-hedral barite grains (Figure 4a) in Zone 2. Considering the low solubility of barite (Hanor, 2000), the formation of these barite grains requires a separate source for Ba^{2+} and SO_4^{2-}. In a seafloor hydrothermal setting, this is best explained by the supply of barium from hydrothermal fluids and sulfate from seawater (Jamieson et al., 2016), although the majority of PACMANUS fluids generally have low SO_4^{2-} concentrations due to subsurface seawater admixing (Reeves et al., 2011). Following this reasoning, the presence of the barite grains likely reflects mixing between the reducing hydrothermal fluid and oxidizing sulfate-bearing seawater that percolates into the porous chimney wall. This is also in agreement with the observation of elevated $\delta^{34}S$ values at ∼13 mm from the inner wall, possibly reflecting the (partial) digestion of sulfate phases with seawater-like $\delta^{34}S$ (21‰). Likewise, the calculated presence of anhydrite, as predicted from the geochemical composition of drilled powders (Table 1), is indicative of seawater entrainment into the chimney wall (Tivey, 2004). The apparent absence of anhydrite in our thick section based on backscattered-electron images may be due to the loss of this mineral during sample preparation.

To test our hypothesis that increased $\delta^{65}Cu$ values are related to the formation of secondary copper sulfides, we used the calculated abundances of bornite and chalcocite in our sample (Table 1) to predict Cu isotope ratios in the chimney powders (Figure 9). For simplicity, we assume that bornite and chalcocite have the same Cu isotopic composition, consistent with the predicted sign magnitudes of isotope fractionation by Liu et al. (2021). For both transects, highly ^{65}Cu-enriched isotopic compositions ($\delta^{65}Cu = 10‰$) are required for bornite and chalcocite to match with the measured isotope ratios in the chimney wall. This isotopic composition is consistent with the shift toward more positive $\delta^{65}Cu$ values from chalcopyrite to chalcocite (Mathur et al., 2018), although the $\delta^{65}Cu$ value is higher than the Cu isotope ratios of secondary copper sulfides in supergene enrichment zones (Mathur & Fantle, 2015), with $\delta^{65}Cu = 6.3‰$ as the maximum value reported for chalcocite so far (Mathur et al., 2010). However, it is plausible that at the grain boundary scale, closed-system (Rayleigh) processes in the chimney wall may lead to more extreme ^{65}Cu-enrichments than those occurring in the open systems of supergene environments. Further work on secondary copper sulfides in hydrothermal chimneys will be required to confirm this.

Although our calculations predict the $\delta^{65}Cu$ values in the chimney reasonably well for Zones 3 and 4, it shows a mismatch for Zones 1 and 2 (Figure 9). This may be partially due to incorrect estimates for the abundance of secondary copper sulfides in Zone 1 as geochemical data predict the presence of bornite and chalcocite whereas these minerals are not observed in backscattered-electron images (Figure 5b). For Zone 2, the model predicts no
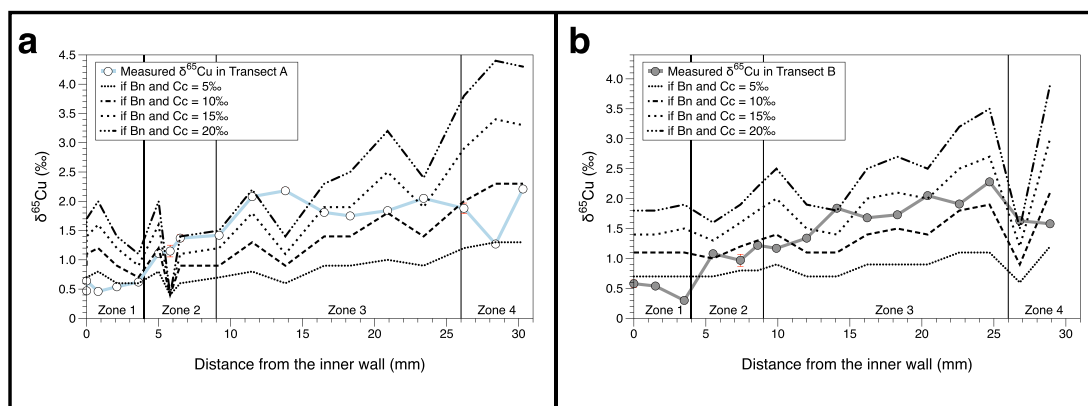
Figure 9. Chimney copper isotope ratios predicted from calculated mineral abundances for transect A (a) and transect B (b) for scenarios where secondary copper sulfides have $\delta^{65}Cu = 5‰$ (dotted line), $\delta^{65}Cu = 10‰$ (dashed line), $\delta^{65}Cu = 15‰$ (dotted line) and $\delta^{65}Cu = 20‰$ (dot-dashed line). Measured $\delta^{65}Cu$ values are indicated in panel (a) with a blue line, and panel (b) with a gray line. Zones 1–4 are delimited by vertical lines.

significant change in $\delta^{65}Cu$ values, which disagrees with the strong increase observed in measured Cu isotope ratios (Figure 9). Interestingly, this zone corresponds to the part of the chimney where barite grains appear but secondary copper sulfides are not yet present (Figure 4). We interpret this to reflect a redox transition zone between the inner wall dominated by reducing hot hydrothermal fluids and the furthest ingress of oxidizing cold seawater into the chimney. Reaction path modeling predicts a significant change in copper speciation with decreasing temperature, changing from $CuCl_2^-$ above 230°C, to $CuHS_{(aq)}$ between 230 and 130°C, and divalent copper species (Cu^{2+} and $CuCl^+$) below 130°C. Although we do not have quantitative constraints on the temperature gradient within the chimney wall, the cooling effect from the inferred intrusion of seawater likely results in reduced temperatures in Zone 2 compared to the high-temperature fluid and consequently, a change in dominant copper species from chloride to sulfide complexes. The magnitude of Cu isotope fractionation between $CuCl_2^-$ and $CuHS_{(aq)}$ is small at temperatures of 200–300°C (up to 0.4‰) (Seo et al., 2007; Sherman, 2013) and can therefore in itself not explain the observed change in $\delta^{65}Cu$. However, Cu sulfide complexing drives local dissolution of chalcopyrite (Reed & Palandri, 2006), which could facilitate isotope fractionation due to the presence of aqueous copper species in the redox gradient of Zone 2. Computational and empirical studies demonstrate that the $\delta^{65}Cu$ of Cu(I) is lower than that of Cu(II) (Ehrlich et al., 2004; Fujii et al., 2013), so that when chalcopyrite reprecipitates after the reduction of Cu(II), it will record higher $\delta^{65}Cu$ values than primary chalcopyrite. Dissolution and re-precipitation of chalcopyrite in the chimney would be further enhanced by low pore fluid pH values within wall interiors, as predicted from reactive transport models (Tivey, 1995, 2004). This increased acidity (in addition to the high primary fluid acidity) may facilitate fluid-solid Cu exchange and oxidation as temperatures decrease over small spatial scales.

5.3. Conceptual Model for Cu Isotope Fractionation in the Chimney Wall

Hydrothermal chimneys continuously evolve and the minerals are in a constant state of re-precipitation as the chimney grows and becomes increasingly thermally self-isolated (Hannington et al., 1995; Tivey, 2004; Tivey et al., 1999). Mineral assemblages in hydrothermal chimneys are not static but can evolve as a result of several processes such as seawater penetrating the chimney structure, progressive growth, thickening of the chimney walls and evolving fluid conduit pathways. These transformations are also clearly demonstrated by the Cu isotope data from the Roman Ruins chimney (Figure 10). After the formation of primary chalcopyrite at high temperature (333°C), seawater enters the chimney and results in oxidative dissolution and reworking of chalcopyrite. The corresponding oxidation of Cu(I) to aqueous Cu(II) leads to the enrichment of ^{65}Cu in the dissolved copper phase (Sherman, 2013; Syverson et al., 2021). Subsequent precipitation of secondary copper sulfides occurs at lower temperatures (270–210°C) when aqueous Cu(II) reaches sulfide-rich and reduced hydrothermal fluids, leading to quantitative reduction of Cu(II) to Cu(I) and precipitation of bornite (Mathur et al., 2018). As a result, the secondary copper sulfides carry a ^{65}Cu-enriched isotope signature compared to the primary chalcopyrite. Our observation that elevated $\delta^{65}Cu$ values correspond to the presence of small barite crystals confirms that these dissolution and re-precipitation reactions occur at the redox gradient between hydrothermal fluids and seawater.
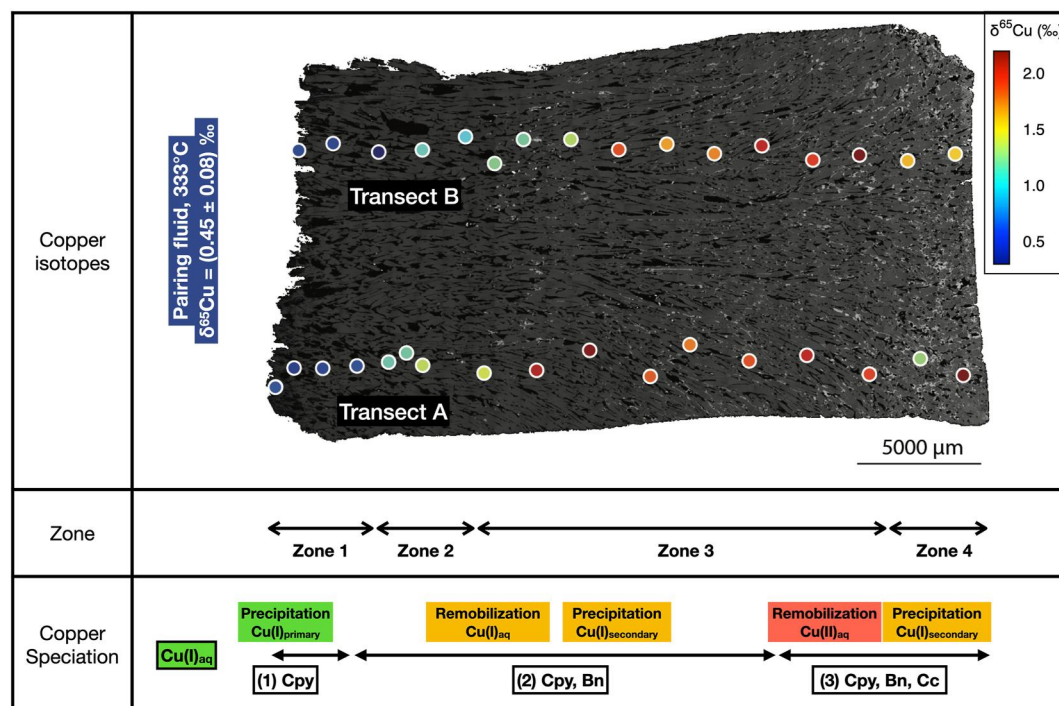
Figure 10. Conceptual model of Cu isotope fractionation in the hydrothermal chimney wall showing zonation and inferred copper speciation from Cu isotope values measured in this study.

In addition, the exclusive presence of chalcocite in the outermost part of the chimney wall is consistent with further oxidation and re-precipitation of secondary sulfides by seawater, as this part of the chimney is likely to be least influenced by hydrothermal fluids and most affected by infiltrating seawater. This seawater mixing would lead to a change in fluid copper speciation from monovalent in the inner wall ($CuCl_2^-$ and $CuHS$) to bivalent (Cu^{2+} and $CuCl^+$) in the outer wall as temperature decreases, resulting in further ^{65}Cu-enrichment in the chalcocite (Mathur et al., 2018). Additionally, as for previous chimney formation models, the oxidizing conditions suggest a pH drop within the wall as secondary minerals form, which could initiate the primary copper phase replacement by secondary copper phases enriched in ^{65}Cu.

6. Conclusion

This study examines copper isotope variations in a hydrothermal chimney from the PACMANUS vent field to assess the preservation of primary hydrothermal fluid Cu isotope signatures in chalcopyrite. Our findings demonstrate that the Cu isotopic composition of the paired hydrothermal fluid is recorded by chalcopyrite in the innermost 5 mm of the chimney wall, and that no significant Cu isotope fractionation occurs during precipitation of chalcopyrite at high temperatures (333°C). However, Cu isotope ratios increase from fluid-like $\delta^{65}Cu$ values to more ^{65}Cu-enriched ratios in the outermost wall. This increase is coupled to an increasing abundance of secondary copper sulfides, reflecting the oxidative dissolution of chalcopyrite and reprecipitation as bornite and chalcocite. We infer that this process results from the intrusion of cold oxidized seawater into the chimney, producing a redox and temperature gradient that leads to isotope fractionation between Cu(I) and Cu(II). The accompanying ^{65}Cu-enrichment of the dissolved copper is recorded by higher $\delta^{65}Cu$ values in the secondary copper phases compared to primary chalcopyrite. Importantly, our study demonstrates that bulk chimney $\delta^{65}Cu$ data are unlikely to reflect the Cu isotopic composition of hydrothermal fluids, and caution must therefore be exercised when subsampling sulfide minerals from chimneys for Cu isotope analyses of primary signatures.

Data Availability Statement

All the data used in this study are available within the tables of the main text and the Supporting Information S1. These data sets are also archived in Samin et al. (2024).

References

Albarede, F. (2004). The stable isotope geochemistry of copper and zinc. *Reviews in Mineralogy and Geochemistry*, *55*(1), 409–427. https://doi.org/10.2138/gsrmg.55.1.409

Bach, W., & Participants, c. (2011). *Report and preliminary results of RV SONNE Cruise SO-216, Townsville (Australia)—Makassar (Indonesia), June 14–July 23, 2011. BAMBUS, back-arc Manus Basin underwater Solfataras., Berichte, Fachbereich Geowissenschaften* (Vol. 280, p. 87). Universität Bremen. Retrieved from http://elib.suub.uni-bremen.de/edocs/00102250-1.pdf

Baconnais, I., Rouxel, O., Dulaquais, G., & Boye, M. (2019). Determination of the copper isotope composition of seawater revisited: A case study from the Mediterranean Sea. *Chemical Geology*, *511*, 465–480. https://doi.org/10.1016/j.chemgeo.2018.09.009

Beaudoin, Y., Scott, S. D., Gorton, M. P., Zajacz, Z., & Halter, W. (2007). Effects of hydrothermal alteration on Pb in the active PACMANUS hydrothermal field, ODP leg 193, Manus Basin, Papua New Guinea: A LA-ICP-MS study. *Geochimica et Cosmochimica Acta*, *71*(17), 4256–4278. https://doi.org/10.1016/j.gca.2007.06.034

Belshaw, N. S., Freedman, P. A., O'Nions, R. K., Frank, M., & Guo, Y. (1998). A new variable dispersion double-focusing plasma mass spectrometer with performance illustrated for Pb isotopes. *International Journal of Mass Spectrometry*, *181*(1), 51–58. https://doi.org/10.1016/s1387-3806(98)14150-7

Berkenbosch, H. A., De Ronde, C. E. J., Paul, B. T., & Gemmell, J. B. (2015). Characteristics of Cu isotopes from chalcopyrite-rich black smoker chimneys at Brothers volcano, Kermadec arc, and Niuatahi volcano, Lau basin. *Mineralium Deposita*, *50*(7), 811–824. https://doi.org/10.1007/s00126-014-0571-y

Binns, R., & Parr, J. (1993). *Report on the PACMANUS-II cruise, RV Franklin, eastern Manus basin, Papua New Guinea* (p. 112). CSIRO 428R.

Borrok, D. M., Wanty, R. B., Ridley, W. I., Wolf, R., Lamothe, P. J., & Adams, M. (2007). Separation of copper, iron, and zinc from complex aqueous solutions for isotopic measurement. *Chemical Geology*, *242*(3–4), 400–414. https://doi.org/10.1016/j.chemgeo.2007.04.004

Craddock, P. R. (2008). Geochemical tracers of processes affecting the formation of seafloor hydrothermal fluids and deposits in the Manus back-arc basin. Ph.D. Thesis. MIT.

Craddock, P. R. (2009). *Geochemical tracers of processes affecting the formation of seafloor hydrothermal fluids and deposits in the Manus back-arc basin*. Massachusetts Institute of Technology.

Crerar, D. A., & Barnes, H. L. (1976). Ore solution chemistry; V, Solubilities of chalcopyrite and chalcocite assemblages in hydrothermal solution at 200° to 350°C. *Economic Geology*, *71*(4), 772–794. https://doi.org/10.2113/gsecongeo.71.4.772

Dekov, V. M., Rouxel, O., Kouzmanov, K., Bindi, L., Asael, D., Fouquet, Y., et al. (2016). Enargite-luzonite hydrothermal vents in Manus back-arc basin: Submarine analogues of high-sulfidation epithermal mineralization. *Chemical Geology*, *438*, 36–57. https://doi.org/10.1016/j.chemgeo.2016.05.021

Ehrlich, S., Butler, I., Halicz, L., Rickard, D., Oldroyd, A., & Matthews, A. (2004). Experimental study of the copper isotope fractionation between aqueous Cu(II) and covellite, CuS. *Chemical Geology*, *209*(3), 259–269. https://doi.org/10.1016/j.chemgeo.2004.06.010

Fujii, T., Moynier, F., Abe, M., Nemoto, K., & Albarède, F. (2013). Copper isotope fractionation between aqueous compounds relevant to low temperature geochemistry and biology. *Geochimica et Cosmochimica Acta*, *110*, 29–44. https://doi.org/10.1016/j.gca.2013.02.007

Gamo, T., Okamura, K., Charlou, J. L., Urabe, T., Auzende, J. M., Ishibashi, J., et al. (1997). Acidic and sulfate-rich hydrothermal fluids from the Manus back-arc basin, Papua New Guinea. *Geology*, *25*(2), 139–142. https://doi.org/10.1130/0091-7613(1997)025<0139:aasrhf>2.3.co;2

Gregory, M. J., & Mathur, R. (2017). Understanding copper isotope behavior in the high temperature magmatic-hydrothermal porphyry environment. *Geochemistry, Geophysics, Geosystems*, *18*(11), 4000–4015. https://doi.org/10.1002/2017gc007026

Hannington, M. D., Jonasson, I. R., Herzig, P. M., & Petersen, S. (1995). *Physical and chemical processes of seafloor mineralization at mid-ocean ridges, seafloor hydrothermal systems: Physical, chemical, biological, and geological interactions* (pp. 115–157). American Geophysical Union.

Hanor, J. S. (2000). Barite–celestine geochemistry and environments of formation. *Reviews in Mineralogy and Geochemistry*, *40*(1), 193–275. https://doi.org/10.2138/rmg.2000.40.4

Humphris, S. E., & Klein, F. (2018). Progress in deciphering the controls on the geochemistry of fluids in seafloor hydrothermal systems. *Annual Review of Marine Science*, *10*(1), 315–343. https://doi.org/10.1146/annurev-marine-121916-063233

Jamieson, J. W., Hannington, M. D., Tivey, M. K., Hansteen, T., Williamson, N. M. B., Stewart, M., et al. (2016). Precipitation and growth of barite within hydrothermal vent deposits from the Endeavour Segment, Juan de Fuca Ridge. *Geochimica et Cosmochimica Acta*, *173*, 64–85. https://doi.org/10.1016/j.gca.2015.10.021

John, S. G., Rouxel, O. J., Craddock, P. R., Engwall, A. M., & Boyle, E. A. (2008). Zinc stable isotopes in seafloor hydrothermal vent fluids and chimneys. *Earth and Planetary Science Letters*, *269*(1–2), 17–28. https://doi.org/10.1016/j.epsl.2007.12.011

Larson, P. B., Maher, K., Ramos, F. C., Chang, Z., Gaspar, M., & Meinert, L. D. (2003). Copper isotope ratios in magmatic and hydrothermal ore-forming environments. *Chemical Geology*, *201*(3–4), 337–350. https://doi.org/10.1016/j.chemgeo.2003.08.006

Liu, S., Li, Y., Liu, J., Yang, Z., Liu, J., & Shi, Y. (2021). Equilibrium Cu isotope fractionation in copper minerals: A first-principles study. *Chemical Geology*, *564*, 120060. https://doi.org/10.1016/j.chemgeo.2021.120060

Maher, K. C., Jackson, S., & Mountain, B. (2011). Experimental evaluation of the fluid–mineral fractionation of Cu isotopes at 250°C and 300°C.

Maréchal, C., & Albarède, F. (2002). Ion-exchange fractionation of copper and zinc isotopes. *Geochimica et Cosmochimica Acta*, *66*(9), 1499–1509. https://doi.org/10.1016/s0016-7037(01)00815-8

Maréchal, C. N., Télouk, P., & Albarède, F. (1999). Precise analysis of copper and zinc isotopic compositions by plasma-source mass spectrometry. *Chemical Geology*, *156*(1–4), 251–273. https://doi.org/10.1016/s0009-2541(98)00191-0

Mason, T. F. D., Weiss, D. J., Chapman, J. B., Wilkinson, J. J., Tessalina, S. G., Spiro, B., et al. (2005). Zn and Cu isotopic variability in the Alexandrinka volcanic-hosted massive sulphide (VHMS) ore deposit, Urals, Russia. *Chemical Geology*, *221*(3–4), 170–187. https://doi.org/10.1016/j.chemgeo.2005.04.011

Mathur, R., Dendas, M., Titley, S., & Phillips, A. (2010). Patterns in the copper isotope composition of minerals in porphyry copper deposits in southwestern United States. *Economic Geology*, *105*(8), 1457–1467. https://doi.org/10.2113/econgeo.105.8.1457

Mathur, R., Falck, H., Belogub, E., Milton, J., Wilson, M., Rose, A., & Powell, W. (2018). Origins of chalcocite defined by copper isotope values. *Geofluids*, *2018*, 1–9. https://doi.org/10.1155/2018/5854829

Mathur, R., & Fantle, M. S. (2015). Copper isotopic perspectives on supergene processes: Implications for the global Cu cycle. *Elements*, *11*(5), 323–329. https://doi.org/10.2113/gselements.11.5.323

Mathur, R., Ruiz, J., Titley, S., Liermann, L., Buss, H., & Brantley, S. (2005). Cu isotopic fractionation in the supergene environment with and without bacteria. *Geochimica et Cosmochimica Acta*, *69*(22), 5233–5246. https://doi.org/10.1016/j.gca.2005.06.022

Mathur, R., Titley, S., Barra, F., Brantley, S., Wilson, M., Phillips, A., et al. (2009). Exploration potential of Cu isotope fractionation in porphyry copper deposits. *Journal of Geochemical Exploration*, *102*(1), 1–6. https://doi.org/10.1016/j.gexplo.2008.09.004

May, T. W., & Wiedmeyer, R. H. (1998). A table of polyatomic interferences in ICP-MS. *Atomic Spectroscopy-Norwalk Connecticut*, *19*, 150–155.

McDermott, J. M., Ono, S., Tivey, M. K., Seewald, J. S., Shanks, W. C., & Solow, A. R. (2015). Identification of sulfur sources and isotopic equilibria in submarine hot-springs using multiple sulfur isotopes. *Geochimica et Cosmochimica Acta*, *160*, 169–187. https://doi.org/10.1016/j.gca.2015.02.016

McDermott, J. M., Sylva, S. P., Ono, S., German, C. R., & Seewald, J. S. (2018). Geochemistry of fluids from Earth's deepest ridge-crest hot-springs: Piccard hydrothermal field, Mid-Cayman Rise. *Geochimica et Cosmochimica Acta*, *228*, 95–118. https://doi.org/10.1016/j.gca.2018.01.021

Preibisch, S., Saalfeld, S., & Tomancak, P. (2009). Globally optimal stitching of tiled 3D microscopic image acquisitions. *Bioinformatics*, *25*(11), 1463–1465. https://doi.org/10.1093/bioinformatics/btp184

Qi, C., Liu, J., Malainey, J., Kormos, L. J., Coffin, J., Deredin, C., et al. (2019). The role of Cu ion activation and surface oxidation for polymorphic pyrrhotite flotation performance in Strathcona Mill. *Minerals Engineering*, *134*, 87–96. https://doi.org/10.1016/j.mineng.2019.01.025

Reed, M. H., & Palandri, J. (2006). Sulfide mineral precipitation from hydrothermal fluids. *Reviews in Mineralogy and Geochemistry*, *61*(1), 609–631. https://doi.org/10.2138/rmg.2006.61.11

Rees, C. E., Jenkins, W. J., & Monster, J. (1978). Sulfur isotopic composition of ocean water sulfate. *Geochimica et Cosmochimica Acta*, *42*(4), 377–381. https://doi.org/10.1016/0016-7037(78)90268-5

Reeves, E. P., Seewald, J. S., Saccocia, P., Bach, W., Craddock, P. R., Shanks, W. C., et al. (2011). Geochemistry of hydrothermal fluids from the PACMANUS, Northeast Pual and Vienna woods hydrothermal fields, Manus Basin, Papua New Guinea. *Geochimica et Cosmochimica Acta*, *75*(4), 1088–1123. https://doi.org/10.1016/j.gca.2010.11.008

Reeves, E. P., Yoshinaga, M. Y., Pjevac, P., Goldenstein, N. I., Peplies, J., Meyerdierks, A., et al. (2014). Microbial lipids reveal carbon assimilation patterns on hydrothermal sulfide chimneys. *Environmental Microbiology*, *16*(11), 3515–3532. https://doi.org/10.1111/1462-2920.12525

Rouxel, O., Fouquet, Y., & Ludden, J. N. (2004). Copper isotope systematics of the Lucky Strike, Rainbow, and Logatchev Sea-floor hydrothermal fields on the Mid-Atlantic Ridge. *Economic Geology*, *99*(3), 585–600. https://doi.org/10.2113/gsecongeo.99.3.585

Rouxel, O., Shanksiii, W., Bach, W., & Edwards, K. (2008). Integrated Fe- and S-isotope study of seafloor hydrothermal vents at East Pacific Rise 9–10°N. *Chemical Geology*, *252*(3–4), 214–227. https://doi.org/10.1016/j.chemgeo.2008.03.009

Samin, A. M., Roerdink, D., Reeves, E., Scheffler, J., Bach, W., Beinlich, A., et al. (2024). Copper isotope ratios across a hydrothermal chimney wall from the Roman Ruins site in the PACMANUS vent field in the Manus Basin, version 1.0 [Dataset]. Interdisciplinary Earth Data Alliance (IEDA). https://doi.org/10.60520/IEDA/113088

Savage, P. S., Moynier, F., Chen, H., Siebert, J., Badro, J., Puchtel, I. S., & Shofner, G. (2015). Copper isotope evidence for large-scale sulphide fractionation during Earth's differentiation. *Geochemical Perspectives Letters*, *1*, 53–64. https://doi.org/10.7185/geochemlet.1506

Schneider, C. A., Rasband, W. S., & Eliceiri, K. W. (2012). NIH image to ImageJ: 25 years of image analysis. *Nature Methods*, *9*(7), 671–675. https://doi.org/10.1038/nmeth.2089

Seewald, J. S., Doherty, K. W., Hammar, T. R., & Liberatore, S. P. (2002). A new gas-tight isobaric sampler for hydrothermal fluids. *Deep-Sea Research I*, *49*(1), 189–196. https://doi.org/10.1016/s0967-0637(01)00046-2

Seewald, J. S., Reeves, E. P., Bach, W., Saccocia, P. J., Craddock, P. R., Shanks, W. C., et al. (2015). Submarine venting of magmatic volatiles in the eastern Manus Basin, Papua New Guinea. *Geochimica et Cosmochimica Acta*, *163*, 178–199. https://doi.org/10.1016/j.gca.2015.04.023

Seo, J. H., Lee, S. K., & Lee, I. (2007). Quantum chemical calculations of equilibrium copper (I) isotope fractionations in ore-forming fluids. *Chemical Geology*, *243*(3–4), 225–237. https://doi.org/10.1016/j.chemgeo.2007.05.025

Shanks, W., Boehlke, J. K., Seal, R., & Humphris, S. (1995). Stable isotopes in mid-ocean ridge hydrothermal systems: Interactions between fluids, minerals, and organisms. *Geophysical Monograph-American Geophysical Union*, *91*, 194.

Sherman, D. M. (2013). Equilibrium isotopic fractionation of copper during oxidation/reduction, aqueous complexation and ore-forming processes. *Predictions From Hybrid Density Functional Theory*, *118*, 85–97. https://doi.org/10.1016/j.gca.2013.04.030

Syverson, D. D., Borrok, D. M., Niebuhr, S., & Seyfried, W. E. (2021). Chalcopyrite-dissolved Cu isotope exchange at hydrothermal conditions: Experimental constraints at 350°C and 50 MPa. *Geochimica et Cosmochimica Acta*, *298*, 191–206. https://doi.org/10.1016/j.gca.2021.02.005

Taylor, B. (1979). Bismarck Sea: Evolution of a back-arc basin. *Geology*, *7*(4), 171–174. https://doi.org/10.1130/0091-7613(1979)7<171:bseoab>2.0.co;2

Thal, J., Tivey, M., Yoerger, D., Jöns, N., & Bach, W. (2014). Geologic setting of PACManus hydrothermal area—High resolution mapping and in situ observations, *355*, 98–114. https://doi.org/10.1016/j.margeo.2014.05.011

Tivey, M. (2004). Environmental conditions within active seafloor vent structures: Sensitivity to vent fluid composition and fluid flow, the subseafloor biosphere at mid-ocean ridges. *American Geophysical Union*, 137–152.

Tivey, M. K. (1995). The influence of hydrothermal fluid composition and advection rates on black smoker chimney mineralogy: Insights from modelling transport and reaction. *Geochimica et Cosmochimica Acta*, *59*(10), 1933–1949. https://doi.org/10.1016/0016-7037(95)00118-2

Tivey, M. K., Stakes, D. S., Cook, T. L., Hannington, M. D., & Petersen, S. (1999). A model for growth of steep-sided vent structures on the Endeavour Segment of the Juan de Fuca Ridge: Results of a petrologic and geochemical study. *Journal of Geophysical Research*, *104*(B10), 22859–22883. https://doi.org/10.1029/1999jb900107

Trefry, J. H., Butterfield, D. B., Metz, S., Massoth, G. J., Trocine, R. P., & Feely, R. A. (1994). Trace metals in hydrothermal solutions from cleft segment on the southern Juan De Fuca Ridge. *Journal of Geophysical Research*, *99*(B3), 4925–4935. https://doi.org/10.1029/93jb02108

Von Damm, K. L., Edmond, J. M., Grant, B., Measures, C. I., Walden, B., & Weiss, R. (1985). Chemistry of submarine hydrothermal solutions at 21°N, East Pacific Rise. *Geochimica et Cosmochimica Acta*, *49*(11), 2197–2220. https://doi.org/10.1016/0016-7037(85)90222-4

Wilckens, F. K., Reeves, E. P., Bach, W., Meixner, A., Seewald, J. S., Koschinsky, A., & Kasemann, S. A. (2018). The influence of magmatic fluids and phase separation on B systematics in submarine hydrothermal vent fluids from back-arc basins. *Geochimica et Cosmochimica Acta*, *232*, 140–162. https://doi.org/10.1016/j.gca.2018.04.023

Woodruff, L. G., & Shanks, W. C. (1988). Sulfur isotope study of chimney minerals and vent fluids from 21°N, East Pacific Rise—Hydrothermal sulfur sources and disequilibrium sulfate reduction. *Journal of Geophysical Research: Solid Earth and Planets*, *93*(B5), 4562–4572. https://doi.org/10.1029/jb093ib05p04562

Zhu, X. K., O'Nions, R. K., Guo, Y., Belshaw, N. S., & Rickard, D. (2000). Determination of natural Cu-isotope variation by plasma-source mass spectrometry: Implications for use as geochemical tracers. *Chemical Geology*, *163*(1–4), 139–149. https://doi.org/10.1016/s0009-2541(99)00076-5